Front. Environ. Sci. Eng. 2018, 12(2): 11
https://doi.org/10.1007/s11783-018-1007-1

RESEARCH ARTICLE

# New insights into mercury removal mechanism on $CeO_2$-based catalysts: A first-principles study

**Ling Li[1], Yu He (✉)[2], Xia Lu[3]**

1 Forestry College, Guizhou University, Guiyang 550025, China
2 Key Laboratory of High-Temperature and High-Pressure Study of the Earth's Interior, Institute of Geochemistry, Chinese Academy of Sciences, Guiyang 550081, China
3 State Key Laboratory of Organic-Inorganic Composites, Beijing Advanced Innovation Center for Soft Matter Science and Engineering, College of Energy, Beijing University of Chemical Engineering, Beijing 100029, China

## HIGHLIGHTS

- $Hg^0$ is chemically adsorbed and fully oxidized by surface oxygen on $CeO_2$.
- HCl promotes the desorption of oxidized Hg on $CeO_2$.
- Surface oxygen is consumed by the H provided by HCl.
- Desorption of oxidized Hg is a rate-determining step.
- Maintenance of sufficient active surface oxygen is another rate-determining step.

## GRAPHIC ABSTRACT

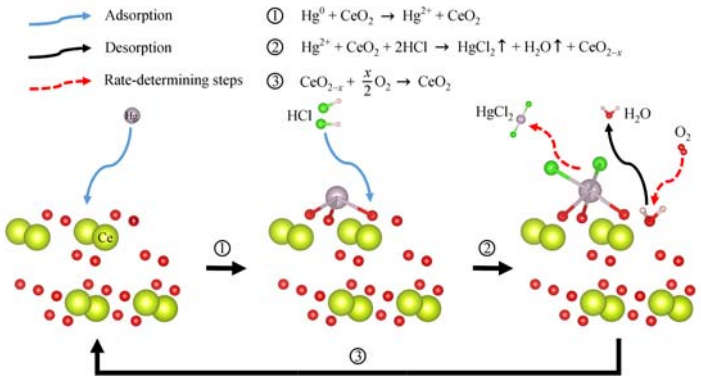


## ARTICLE INFO

*Article history:*
Received 29 June 2017
Revised 28 September 2017
Accepted 7 October 2017
Available online 18 November 2017

*Keywords:*
Elemental mercury removal
Surface adsorption
Ceria
First-principles calculations

## ABSTRACT

First-principles calculations were performed to investigate the mechanism of $Hg^0$ adsorption and oxidation on $CeO_2$(111). Surface oxygen activated by the reduction of $Ce^{4+}$ to $Ce^{3+}$ was vital to $Hg^0$ adsorption and oxidation processes. $Hg^0$ was fully oxidized by the surface lattice oxygen on $CeO_2$(111), without using any other oxidizing agents. HCl could dissociate and react with the Hg adatom on $CeO_2$(111) to form adsorbed Hg–Cl or Cl–Hg–Cl groups, which promoted the desorption of oxidized Hg and prevented $CeO_2$ catalyst deactivation. In contrast, O–H and H–O–H groups formed during HCl adsorption consumed the active surface oxygen and prohibited Hg oxidation. The consumed surface oxygen was replenished by adding $O_2$ into the flue gas. We proposed that oxidized Hg desorption and maintenance of sufficient active surface oxygen were the rate-determining steps of $Hg^0$ removal on $CeO_2$-based catalysts. We believe that our thorough understanding and new insights into the mechanism of the $Hg^0$ removal process will help provide guidelines for developing novel $CeO_2$-based catalysts and enhance the $Hg^0$ removal efficiency.



## 1 Introduction

As an air-toxic metal, mercury is of major concern due to its volatility, persistence, and bioaccumulation as methylmercury in the environment and its neurological health impacts [1,2]. Nowadays, emissions from coal combustion processes constitute a significant amount of mercury released into the atmosphere [3]. Mercury exists in three different forms: oxidized mercury ($Hg^{2+}$), particulate mercury (Hg(p)), and elemental mercury ($Hg^0$) [4,5]. $Hg^0$ is the most abundant form in the atmosphere, and it is also the most difficult to remove due to its high volatility, low reactivity, and low solubility [3,6]. Therefore, enhancing the sorption and oxidation of $Hg^0$ on particle surfaces is necessary for $Hg^0$ emission control.

✉ Corresponding author
E-mail: heyu@mail.gyig.ac.cn

Various sorbents or catalysts, including activated carbon, metal oxides, metal sulfides, and pure metals, may be used in the combustion flue gas environment to capture and oxidize $Hg^0$ [6–8]. Among recently developed sorbents and catalysts, Ce-based oxides are promising as selective catalytic reduction catalysts for the removal of $Hg^0$ at low flue gas temperatures [9–14]. Hg oxidation over the $CeO_2$-$TiO_2$ catalyst in the simulated flue gas was reported to be higher than 90% in the temperature range of 200°C–250°C [10]. The oxidation of $Hg^0$ can be promoted in the absence of $O_2$, HCl, and NO owing to the presence of surface oxygen on $CeO_2$. High $Hg^0$ conversion rates by $CeO_2$-$MoO_3$ catalysts at different temperatures (150°C, 250°C, 350°C, and 450°C) have been reported by Chang et al. [12]. The reduction of $Ce^{4+}$ to $Ce^{3+}$ can provide a large amount of surface lattice oxygen, which could be used for $Hg^0$ adsorption and oxidation. In addition, transition metals can be well dispersed on the $CeO_2$ surface, which enhances the reduction of $Ce^{4+}$ to $Ce^{3+}$ and promotes the catalytic reactivity of $CeO_2$ [15–18].

For the $Hg^0$ oxidation reaction in the coal-fired flue gas, HCl is the most important oxidizing agent because the HCl concentration is higher than the $Cl_2$ concentration [9–12]. The oxidation efficiency of $CeO_2$-based catalysts increases significantly due to the presence of HCl. The overall reaction for the catalytic oxidation of $Hg^0$ is shown by the following equation:

$$Hg^0 + 2HCl + 1/2O_2 \leftrightarrow HgCl_2 + H_2O \quad (1)$$

On the contrary, $NH_3$ exhibited an inhibitory effect on $Hg^0$ adsorption because it consumed the surface absorption sites [12–14]. The mechanism of $Hg^0$ adsorption and oxidation on the $CeO_2$-based catalyst is quite complicated; therefore, a thorough investigation by theoretical methods is necessary.

Quantum chemical methods based on density functional theory (DFT) have been utilized to elucidate the $Hg^0$ adsorption and oxidation processes on different substrates such as Au(111), α-$Fe_2O_3(1\bar{1}02)$, $MnO_2$(110), and $CeO_2$ (111) [19–23]. Lim et al. reported a three-step oxidation mechanism that oxidized Hg to HgCl, and then to $HgCl_2$. By calculating the barrier energy, they deduced that the oxidation of HgCl to $HgCl_2$ was the rate-limiting step [19,20]. Jung et al. showed that $Hg^0$ was physically adsorbed on α-$Fe_2O_3(1\bar{1}02)$ and the absorption strength was enhanced by the presence of Cl [21]. Zhang et al. calculated the $Hg^0$ adsorption energy on $MnO_2$(110) and showed that $Hg^0$ was strongly adsorbed on the $MnO_2$ surface via chemisorption [22]. They also investigated the $Hg^0$ adsorption and oxidation process on $CeO_2$(111) [23] and determined the entire Hg oxidation reaction pathway of Hg to HgCl, and then to $HgCl_2$. They suggested that $HgCl_2$ formation was the rate-determining step. Nevertheless, the standard energy functionals of generalized gradient approximation (GGA) without adding a Hubbard U term do not allow for a reliable description of reduced ceria, i.e., when an electron is localized on the Ce-4f states leading to a $Ce^{3+}$ ion [24–26]. As a result, their calculations failed to take into account the effect of $Ce^{4+}$ reduction to $Ce^{3+}$ and the active surface oxygen of $CeO_2$, both of which are important for elucidating the surface catalytic process of $CeO_2$. Here, we considered the strong correlation of the Ce-4f states with the DFT + U protocol and investigated the mechanism of $Hg^0$ adsorption and oxidation on $CeO_2$(111). The effect of $Ce^{4+}$ reduction to $Ce^{3+}$, active surface oxygen, and participation of HCl in the $Hg^0$ oxidation process are extensively discussed.

## 2 Computational details

We applied spin-polarized density functional theory (DFT) plane wave calculations as implemented in the Vienna ab initio simulation package (VASP) with the projector augmented wave method (PAW) [27–30]. The exchange-correlation energy term was treated using the Perdew–Burke–Ernzerhof (PBE) GGA in conjunction with the interpolation formula [31,32]. A reliable description of both stoichiometric and reduced ceria-based materials was achieved by adding a Hubbard U correction into the GGA energy term that described the localized f electrons on Ce ions. The optimal value of U correction of Ce ions, $U_{eff}$, was approximately 5.0 eV, as discussed by Zhang et al. [33]. Therefore, $U_{eff}$ = 4.5 eV was chosen after the linear-response approach of Cococcioni and de Gironcoli, as suggested by Fabris et al. [34]. In our calculations, a plane wave representation of the wave function was applied with a cut-off energy of 500 eV. The convergence of ceria reached $1.0 \times 10^{-4}$ eV in the self-consistent field (SCF) energy, and $1 \times 10^{-3}$ eV and 0.05 eV/Å in the total energy and atomic forces, respectively, when we optimized the structures. The electron configurations of O-$2s^2 2p^2$, Hg-$5d^{10}6s^2$, H-$1s^1$, and Cl-$3s^2 3p^5$ were chosen as the valence electrons. Different configurations were used for Ce atoms in the calculations, including $5s^2 5p^6 6s^2 5d^{14} f^1$ and $6s^2 5d^{14} f^1$.

The $CeO_2$(111) surface was modeled using a p($2 \times 2$) 9-layer slab (12 $CeO_2$ units per supercell), where the top three layers were relaxed for structure optimization. The vacuum region between the slabs was 20 Å, which was verified to sufficiently avoid the interactions between the slabs (Fig. 1). The Brillouin zone was sampled with a $3 \times 3 \times 1$ k-points mesh, generated by the Monkhorst-Pack algorithm. The adsorption energies ($E_{ads}$) were calculated by $E_{ads} = E_{(surface - adsorbate)} - E_{(surface)} - E_{(adsorbate)}$, where $E_{(surface - adsorbate)}$, $E_{(surface)}$, and $E_{(adsorbate)}$ were the calculated electronic energies of the adsorbed species on the surface, bare surface, and adsorbate in gas phase, respectively. Bader charge analysis was employed to calculate the charge transfer of the reactions based on the zero flux surfaces method [35,36]. Bonding charge density

was evaluated by calculating the charge difference as $\rho = \rho_{(surface + absorbate)} - \rho_{(surface)} - \rho_{(absorbate)}$, where $\rho_{(surface + adsorbate)}$, $\rho_{(surface)}$, and $\rho_{(adsorbate)}$ were the charge density of adsorbed species on the surface, bare surface, and adsorbate, respectively.

## 3 Results and discussion

### 3.1 $Hg^0$ adsorption and oxidation on $CeO_2(111)$

A single Hg atom was placed at various active sites on $CeO_2(111)$, including Ce-top (Ce*t*), O-top (O*t*), Ce-Ce bridge (Ce*b*), O-O bridge (O*b*), and O-hollow (*h*) positions, to simulate mercury adsorption on $CeO_2(111)$ at low concentrations (Fig. 1(b)). In each case, the Hg–Hg interactions were weakened by the lower surface coverage. The calculated adsorption energies and Hg–O bond lengths are given in Table 1. The different valence electron configurations of Ce atoms resulted in a significant difference in the calculations. When the $5s^25p^66s^25d^14f^1$ electron configuration of Ce atoms was used, the interaction between Hg and $CeO_2(111)$ was quite weak, as indicated by the large distance (3.85 Å) between the Hg atom and its nearest O atom at the Ce-top site, as well as the relatively large adsorption energy (–4.27 kJ/mol). According to Bader charge analysis, this valance electron configuration gave the oxidation states of adatom Hg at various adsorption sites in the range of 11.95–11.96 e. This was quite close to the Bader charge of atomic Hg (11.96 e) and indicated physical absorption of Hg on $CeO_2(111)$. This result was consistent with previous research [23], where the adsorption mechanism of $Hg^0$ on $CeO_2$ was proposed as physisorption. However, the experimental observations disagreed with this hypothesis. $CeO_2$-based catalysts are known for their capability to effectively remove $Hg^0$ at relatively low temperatures without using oxidizing agents such as $O_2$, HCl, and NO [9–11]. X-ray

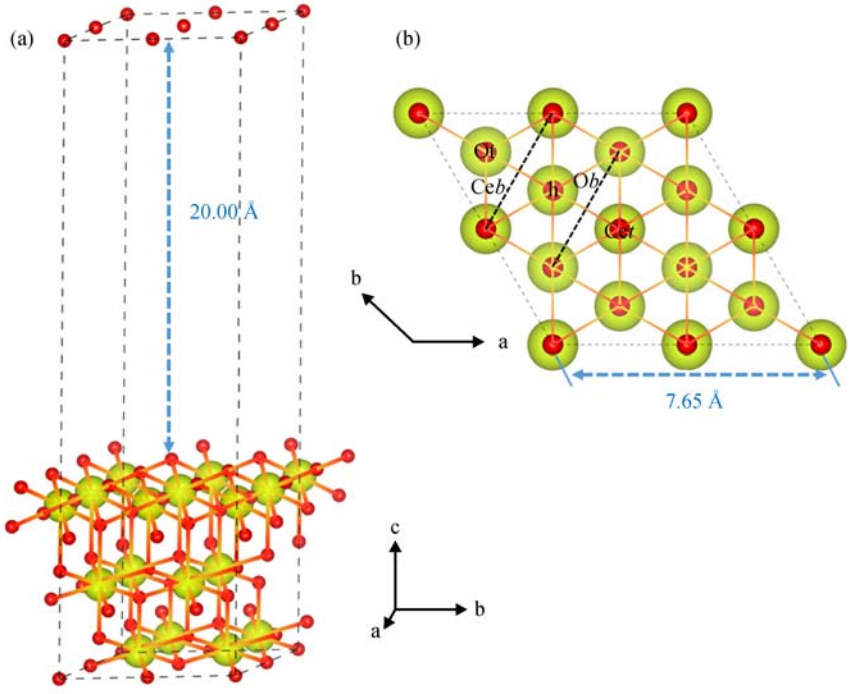


**Fig. 1** $CeO_2(111)$-p(2 × 2) 9-layer slab: (a) side and (b) top views, in which yellow and red spheres represent Ce and O atoms, respectively. Ce*t*, Ce*b*, O*b*, O*t,* and *h* correspond to active sites at Ce-top, Ce-bridge, O-top, O-bridge and O hollow positions

**Table 1** Adsorption energies ($E_{ads}$) and equilibrium distances of a Hg adatom on the $CeO_2(111)$

| Adsorption site | $5s^25p^66s^25d^14f^1$ | | $6s^25d^14f^1$ | |
|---|---|---|---|---|
| | $E_{ads}$ (kJ/mol) | $R_{Hg-O}$ (Å) | $E_{ads}$ (kJ/mol) | $R_{Hg-O}$ (Å) |
| Ce-top | –4.27 | 3.85 | –130.21 | 2.32 |
| Ce-bridge | 18.52 | 2.57 | –201.46 | 2.25 |
| O-top | –2.26 | 3.42 | –59.64 | 2.18 |
| O-bridge | –3.50 | 3.83 | –201.43 | 2.25 |
| O-hollow | –3.56 | 3.80 | –201.49 | 2.25 |

photoelectron spectroscopy (XPS) characterization provided direct evidence for Hg oxidation on the $CeO_2$ surface [9]. The valence electron configuration, $5s^25p^66s^25d^14f^1$, failed to describe the surface properties of $CeO_2$.

When only the outmost electrons were considered as the valence electrons, i.e., the $6s^25d^14f^1$ configuration, the calculated adsorption energy of Hg at the O hollow sites was –201.49 kJ/mol (labeled as *h* in Fig. 1(b)). At this optimized position, the Hg atom was exactly at the centroid of the three neighboring O atoms with a Hg–O bond length of 2.25 Å in the first coordinate layer (Fig. 2). The Hg atoms initially located at Ce*b* and O*b* also moved to the *h* site to minimize the adsorption energies during this structural optimization (Table 1). Bader charge analysis suggested that the electrons were transferred from Hg to $CeO_2(111)$, resulting in a value as low as 11.25 e, which was smaller than that of the atomic Hg. The oxidation states of Hg in HgO, HgCl, and $HgCl_2$ were also calculated (Table 2). According to the calculated results, the oxidation state of adatom Hg on $CeO_2(111)$ was quite close to that of $HgCl_2$. This consistency implied a strong interaction between the Hg and $CeO_2$ substrate. As a result, the Hg adsorption mechanism was considered to involve chemisorption and $Hg^0$ was fully oxidized when adsorbed on a bare $CeO_2(111)$ surface.

Bader charge analysis was also conducted on bulk $CeO_2$ and $Ce_2O_3$ to determine the oxidation states of Ce atoms after Hg adsorption. The resulting charge was 8.71 e and 8.80 e for $CeO_2$ ($Ce^{4+}$) and $Ce_2O_3$ ($Ce^{3+}$), respectively (Table 2). This charge value was within the range of 8.71–8.80 e after Hg adsorption, which suggested the partial reduction of $Ce^{4+}$. The valance further approached the reduction state ($Ce^{3+}$) at the adsorption sites of Ce*t*, Ce*b*, O*b*, and *h,* which indicated a strong $Ce^{4+}/Ce^{3+}$ reduction process during Hg adsorption. The same conclusion was obtained from the charge density difference between the adsorbate system and the isolated molecule slab induced by the adsorption of $Hg^0$ on $CeO_2(111)$. As shown in Fig. 3, the interaction between the adatom Hg and the surface oxygen was much stronger than the Ce–O interactions. This interaction became more evident when compared to that of the bare $CeO_2(111)$ before $Hg^0$ adsorption (Fig. 3(b)). Therefore, it was concluded that the reduction of $Ce^{4+}$ to $Ce^{3+}$ on $CeO_2(111)$ activated the surface oxygen atoms to chemically adsorb and oxidize $Hg^0$. The advantage of using $CeO_2$ as a catalyst was illuminated when the calculated Hg adsorption energies were compared to those on other substrates such as Au(111), $MnO_2(110)$, and $\alpha$-$Fe_2O_3(1\bar{1}02)$ [19–22]. The minimum adsorption energies of Hg on Au(111), $MnO_2(110)$, and $\alpha$-$Fe_2O_3(1\bar{1}02)$ were –9.93, –78.32, and –41.84 kJ/mol, respectively, which were much higher than the adsorption energy on $CeO_2(111)$. $CeO_2(111)$ showed excellent $Hg^0$ adsorption capability because of its highly active and oxygen-terminated surface as a result of the $Ce^{4+}/Ce^{3+}$ reduction, which enabled spontaneous Hg oxidation.

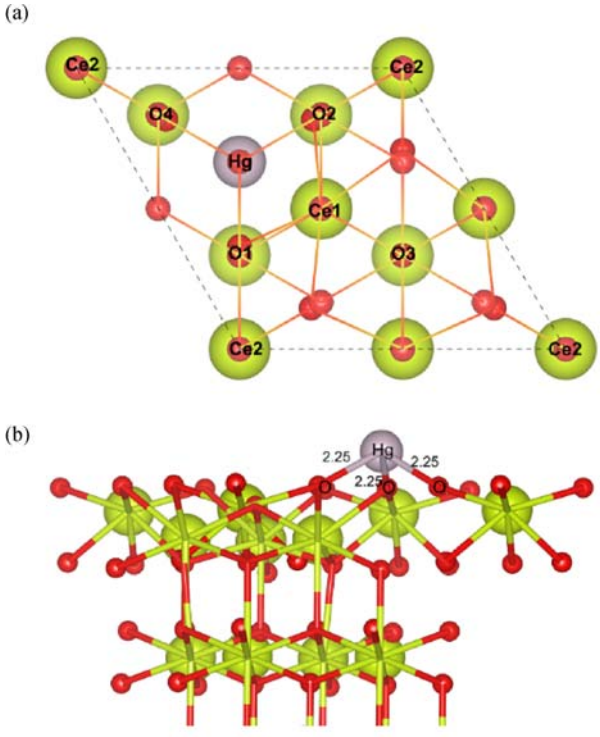


**Fig. 2** Most stable configuration of Hg-adsorbed $CeO_2(111)$: (a) top and (b) side views. Gary, yellow, and red spheres represent Hg, Ce, and O atoms, respectively. Active sites Ce1, Ce2, O1, O2, O3, and O4 are labeled

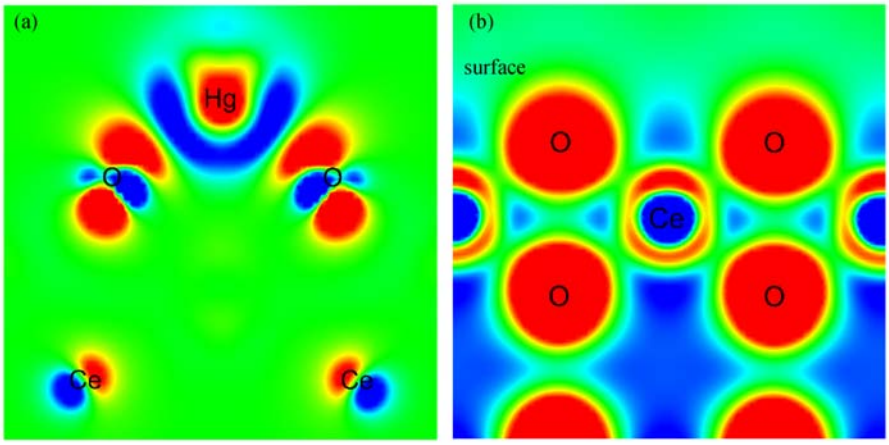


**Fig. 3** Charge density difference for (a) Hg adsorption at the O-hollow site and (b) bare $CeO_2$(111). Red and blue colors represent charge accumulation and depletion, accordingly

**Table 2** Calculated Bader charges of Hg, Ce, and O in various compounds and configurations

| Compounds/Configurations | Hg (e) | Ce (e) | O (e) |
|---|---|---|---|
| Hg (g) | 11.96 | | |
| HgO (g) | 11.60 | | |
| HgCl (g) | 11.57 | | |
| $HgCl_2$ (g) | 11.24 | | |
| $CeO_2$ (s) | | 8.71 | 7.14 |
| $Ce_2O_3$ (s) | | 8.80 | 7.45 |
| Ce-top[a)] | 11.96 | 8.73 | 7.12 |
| Ce-bridge[a)] | 11.96 | 8.71 | 7.13 |
| O-top[a)] | 11.95 | 8.72 | 7.13 |
| O-bridge[a)] | 11.95 | 8.73 | 7.12 |
| O-hollow[a)] | 11.95 | 8.72 | 7.11 |
| Ce-top[b)] | 11.23 | 8.80 | 7.25 |
| Ce-bridge[b)] | 11.24 | 8.77 | 7.22 |
| O-top[b)] | 11.63 | 8.75 | 7.19 |
| O-bridge[b)] | 11.24 | 8.78 | 7.22 |
| O-hollow[b)] | 11.25 | 8.78 | 7.22 |

Notes: a) Hg/$CeO_2$(111) Ce-$5s^25p^66s^25d^14f^1$; b) Hg/$CeO_2$(111) Ce-$6s^25d^14f^1$

Based on these conclusions, which were consistent with experimental results, the valence electron configuration of $6s^25d^14f^1$ was used for subsequent calculations.

### 3.2 Effects of HCl on Hg adsorption and oxidation on $CeO_2$(111)

HCl is the predominant flue gas species that promotes $Hg^0$ oxidation on $CeO_2$-based catalysts because the main oxidized mercury species in coal combustion flue gas exists as $HgCl_2$. However, the prohibitive effect of HCl was also observed on the $CeO_2$–$TiO_2$ sorbent [11]. The mechanism of HCl in $Hg^0$ oxidation on $CeO_2$-based catalysts is complicated and poorly understood. We investigated the HCl adsorption and oxidation behavior on Hg-adsorbed $CeO_2$(111). The adatom Hg at an O-hollow site was chosen as the substrate for HCl adsorption, and two HCl molecules were placed at various adsorption sites. There were six stable adsorption configurations (Fig. 4), and the initial adsorption sites in each configuration for two HCl molecules were O1O2-top, O3O4-top, O3-top, O4-top, Ce1Ce2-top, and CeHg-top. The oxygen and cerium atoms are labeled in Fig. 2(a). HCl dissociation occurred at the active sites of O1O2-top, O3O4-top, O3-top, O4-top, and Ce1Ce2-top. In these configurations, H atoms from dissociated HCl were adsorbed by the nearest O atoms on the $CeO_2$ surface to form H–O or H–O–H groups with H–O bond lengths of approximately 1.0 Å (Fig. 4). Simultaneously, the dissociated Cl atoms bonded to adatom Hg in adsorbed Hg–Cl or Cl–Hg–Cl groups with Hg–Cl bond lengths that ranged from 2.31 to 2.93 Å. These adsorbed Hg–Cl and Cl–Hg–Cl groups remained bonded to 1–3 surface oxygen atoms, which resulted in various bond lengths (Fig. 4). In contrast to bare Hg adsorption, the Hg–O bonds were typically lengthened after the adsorption of Cl atoms and indicated weaker interactions between the Cl–Hg–Cl groups and $CeO_2$(111). These weaker interactions promoted the desorption process that led to the oxidation of Hg to $HgCl_2$. Our calculations showed that Hg was fully oxidized by the surface oxygen on $CeO_2$. However, this process consumed active surface oxygen and led to catalyst deactivation if the oxidized Hg was not removed from the catalyst surface in the gas phase. As shown in Fig. 2(b), the adatom Hg bonded with three nearby oxygens, which made it extremely difficult to desorb the oxidized Hg in the form of HgO. It was much easier to desorb the Cl–Hg–Cl groups from $CeO_2$(111) while maintaining the population of active surface oxygen, and the activity of $CeO_2$ catalyst was recovered. In the case

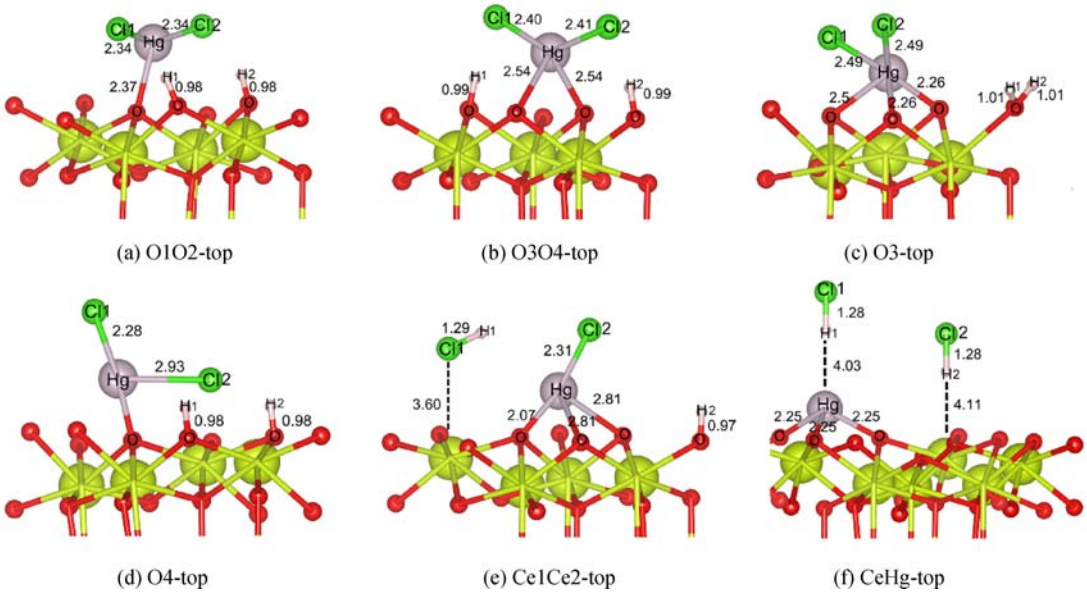


**Fig. 4** Side views of the optimized configurations of two HCl on the Hg-adsorbed $CeO_2$(111): (a) O1O2-top, (b) O3O4-top, (c) O3-top, (d) O4-top, (e) Ce1Ce2-top, (f) CeHg-top

**Table 3** Adsorption energies ($E_{ads}$) of two HCl molecules on Hg-adsorbed $CeO_2$(111), and the calculated Bader charges of Hg, H, Cl, and O (bonded with H) in various compounds and configurations

| Compounds | $E_{ads}$ (kJ/mol) | Hg (e) | H1 (e) | H2 (e) | Cl1 (e) | Cl2 (e) | O (e) |
|---|---|---|---|---|---|---|---|
| HgCl (g) | | 11.57 | | | 7.38 | | |
| $HgCl_2$ (g) | | 11.24 | | | 7.35 | 7.35 | |
| HCl (g) | | | 0.67 | | 7.30 | | |
| $H_2O$ (g) | | | 0.12 | 0.12 | | | 7.73 |
| O1O2-top[a)] | –413.63 | 11.23 | 0.34 | 0.33 | 7.42 | 7.43 | 7.45 |
| O3O4-top[a)] | –419.86 | 11.19 | 0.31 | 0.35 | 7.46 | 7.45 | 7.48 |
| O3-top[a)] | –277.50 | 11.04 | 0.38 | 0.38 | 7.43 | 7.43 | 7.35 |
| O4-top[a)] | –430.18 | 11.20 | 0.31 | 0.37 | 7.36 | 7.72 | 7.41 |
| Ce1Ce2-top[a)] | –281.68 | 11.22 | 0.65 | 0.42 | 7.33 | 7.40 | 7.37 |
| CeHg-top[a)] | –26.95 | 11.24 | 0.73 | 0.73 | 7.25 | 7.26 | |

Notes: a) 2HCl/Hg/$CeO_2$

of the CeHg-top, HCl molecules were physically adsorbed on the top of Ce and Hg. However, the calculated adsorption energies listed in Table 3 showed that this physical adsorption was not stable. As a result, the active surface oxygen determined HCl dissociation and promoted the formation of Hg–Cl or Cl–Hg–Cl groups.

The charge transfer during HCl adsorption on Hg-absorbed $CeO_2$(111) was evaluated by Bader charge analysis and charge density difference. The H and Cl atom labels from Fig. 4 are maintained in the subsequent discussion. The calculated Bader charges of each species of HgCl, $HgCl_2$, HCl, and $H_2O$ were used as a baseline to evaluate the oxidation states of Hg, Cl, and H (Table 3). Bader charge analysis of Hg and Cl showed that a significant charge transfer occurred after HCl adsorption due to the strong interaction between Hg and Cl atoms. A similar conclusion was deduced from the profound charge accumulation between Hg and Cl (Fig. 5). The calculated Bader charge of H adsorbed on surface oxygen was approximately 0.35 e, which was in the range of the charge between HCl and $H_2O$ and indicated a relatively strong interaction. Two hydrogens were bonded to one surface oxygen in the case of the O3-top with a H–O–H angle of about 100°, which was similar to that in a $H_2O$ molecule (Fig. 5(c)). However, the charge distribution of this H–O–H group was different from isolated $H_2O$, and this group was still chemically adsorbed on the $CeO_2$ surface. The Bader charges of H and Cl for HCl physisorption in

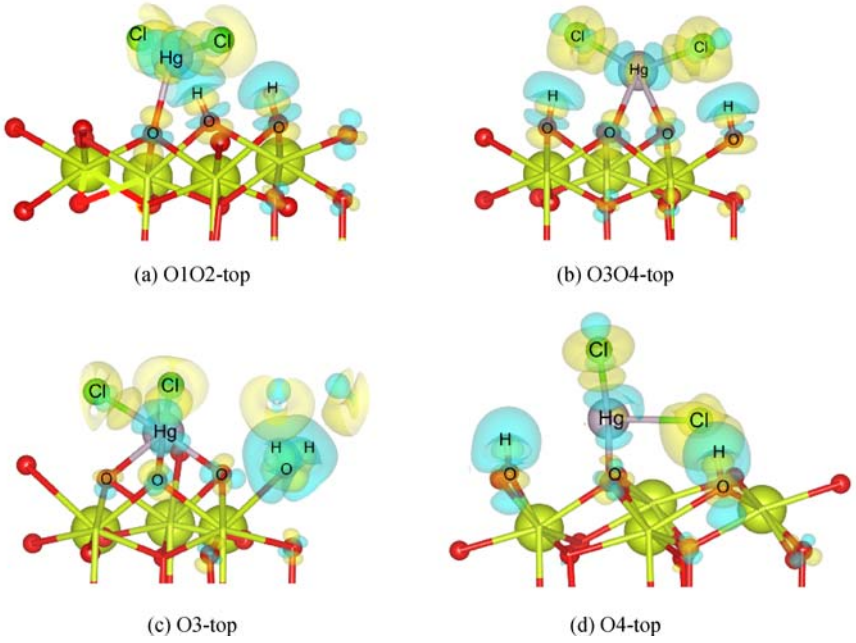


**Fig. 5** Charge density difference for two HCl adsorptions on Hg-adsorbed $CeO_2(111)$: (a) O1O2-top, (b) O3O4-top, (c) O3-top, (d) O4-top. The isosurfaces were calculated at 0.05 $bohr^{-3}$

Ce1Ce2-top and CeHg-top were the same as those in an isolated HCl molecule.

### 3.3 $Hg^0$ oxidation mechanism and efficiency on $CeO_2(111)$

The active surface oxygen resulting from $Ce^{4+}/Ce^{3+}$ reduction determined the $Hg^0$ adsorption and oxidation on $CeO_2(111)$. Bader charge analyses also revealed that $Hg^0$ was fully oxidized without other oxidizing agents, which was plausibly consistent with the experimental results [9–11]. Our simulation temperature of these surface reactions was at 0 K; therefore, the barrier energy of $Hg^0$ adsorption and oxidation on $CeO_2(111)$ was extremely low. This eliminated the need for other catalysts to promote this procedure. HCl was a highly efficient agent for $Hg^0$ removal on $CeO_2$-based catalysts [10]. Our simulation results demonstrated that HCl easily dissociated and reacted with the Hg adatom on $CeO_2(111)$ to form Hg–Cl or Cl–Hg–Cl surface adsorbed groups. The oxidation state of Hg was maintained during this reaction. HCl absorption decreased the bonding energy between oxidized Hg and $CeO_2(111)$ to allow facile desorption of Hg–Cl or Cl–Hg–Cl groups as HgCl or $HgCl_2$ molecules, respectively, above 200°C. $Ce^{3+}$ was simultaneously oxidized back to $Ce^{4+}$. The removal of oxidized Hg bonded to three nearby O atoms without HCl was difficult, which led to the consumption of surface oxygen and deactivation of the $CeO_2$ catalyst. Rather than Hg oxidation as proposed in theoretical work with other catalysts [19–22], HCl facilitated the release of oxidized Hg ions and restored active surface oxygen for further $Hg^0$ oxidation in the case of $CeO_2$.

In addition to HCl, $H_2S$ was also reported as an effective syngas for $Hg^0$ removal at a low temperature [11]. $H_2S$ can react with surface oxygen on $CeO_2$ to generate active surface sulfur, which can then react with $Hg^0$ to form HgS. The interactions between $CeO_2$ and adsorbed active sulfur were weaker than those between $CeO_2$ and active surface oxygen; hence, HgS removal was facile and occurred at temperatures as low as 150°C. Therefore, oxidized Hg desorption was one of the rate-determining steps of $Hg^0$ removal from $CeO_2$-based catalysts.

Additionally, HCl prohibited Hg removal from $CeO_2$-based catalysts. This effect was easily rationalized from our simulated results. As shown in Fig. 4, hydrogen from the dissociated HCl bonded with the surface oxygen to form O–H or H–O–H groups. These groups deactivated the surface oxygen and resulted in lower $Hg^0$ removal efficiency. The H–O–H groups were desorbed as $H_2O$ and caused irreversible loss of active surface oxygen. However, the addition of gas-phase $O_2$ compensated for surface oxygen consumption. It was reported that the $Hg^0$ removal efficiency reached as high as 100% when 4% $O_2$ and 10 ppm HCl were added to the flue gas [9]. The presence of $O_2$ replenished the consumed active surface oxygen to maintain a high surface concentration. The methods used to maintaining the high concentrations of surface oxygen are critical to the Hg removal reaction.

## 4 Conclusions

A first-principles method was used to investigate the $Hg^0$ adsorption and oxidation mechanism on $CeO_2(111)$. Active surface oxygen was provided by $Ce^{4+}$ reduction to $Ce^{3+}$ and was essential for $Hg^0$ adsorption and oxidation on the $CeO_2$ surface. $Hg^0$ was fully oxidized and chemically adsorbed on $CeO_2(111)$ without the use of additional oxidizing agents. This result was plausibly consistent with the experimental observations. The adsorption of HCl molecules promoted the desorption of oxidized Hg from $CeO_2(111)$ in the form of $HgCl_2$ and restored active surface oxygen for further $Hg^0$ oxidation. By contrast, the O–H and H–O–H groups formed during HCl adsorption consumed the active surface oxygen and prohibited Hg adsorption. Gas-phase $O_2$ successfully replenished the consumed surface oxygen on $CeO_2$. The desorption of oxidized Hg and the maintenance of sufficient active surface oxygen were the rate-determining steps of $Hg^0$ removal from $CeO_2$-based catalysts. We provided a thorough mechanistic understanding to enhance the development of novel $CeO_2$-based catalysts and removal efficiency of $Hg^0$.

**Acknowledgements** This research was partially supported by the State Key Laboratory of Organic-Inorganic Composites (oic-201701011), the Fundamental Research Funds for the Central Universities (ZY1720), and Beijing Advanced Innovation Center for Soft Matter Science and Engineering. We are grateful to Dr. Yang Sun and Dr. Hsien-Chieh Chiu for fruitful discussion.

**Conflict of interest statement** The authors declare no competing financial interest.

## References

1. Pavlish J H, Sondreal E A, Mann M D, Olson E S, Galbreath K C, Laudal D L, Benson S A. Status review of mercury control options for coal-fired power plants. Fuel Processing Technology, 2003, 82 (2-3): 89–165
2. Mergler D, Anderson H A, Chan L H, Mahaffey K R, Murray M, Sakamoto M, Stern A H. Methylmercury exposure and health effects in humans: A worldwide concern. Ambio, 2007, 36(1): 3–11
3. Wu Q, Wang S, Li G, Liang S, Lin C J, Wang Y, Cai S, Liu K, Hao J. Temporal trend and spatial distribution of speciated atmospheric mercury emissions in China during 1978–2014. Environmental Science & Technology, 2016, 50(24): 13428–13435
4. Presto A A, Granite E J. Survey of catalysts for oxidation of mercury in flue gas. Environmental Science & Technology, 2006, 40(18): 5601–5609
5. Galbreath K C, Zygarlicke C J. Mercury speciation in coal combustion and gasification flue gases. Environmental Science & Technology, 1996, 30(8): 2421–2426
6. Wilcox J, Rupp E, Ying S C, Lim D H, Negreira A S, Kirchofer A, Feng F, Lee K. Mercury adsorption and oxidation in coal combustion and gasification processes. International Journal of Coal Geology, 2012, 90–91: 4–20
7. Monnell J D, Vidic R D, Gang D, Karash A, Granite E J. Recent Advances in Trace Metal Capture Using Micro and Nano-Scale Sorbents. In: Proceedings of the 23rd Pittsburgh Coal Conference. Pittsburgh, PA: University of Pittsburgh, 2006
8. Granite E J, Pennline H W, Hargis R A. Novel sorbents for mercury removal from flue gas. Industrial & Engineering Chemistry Research, 2000, 39(4): 1020–1029
9. Hua X Y, Zhou J S, Li Q, Luo Z Y, Cen K F. Gas-phase elemental mercury removal by $CeO_2$ impregnated activated coke. Energy & Fuels, 2010, 24(10): 5426–5431
10. Li H, Wu C Y, Li Y, Zhang J. $CeO_2$-$TiO_2$ catalysts for catalytic oxidation of elemental mercury in low-rank coal combustion flue gas. Environmental Science & Technology, 2011, 45(17): 7394–7400
11. Zhou J, Hou W, Qi P, Gao X, Luo Z, Cen K. $CeO_2$-$TiO_2$ sorbents for the removal of elemental mercury from syngas. Environmental Science & Technology, 2013, 47(17): 10056–10062
12. Chang H, Wu Q, Zhang T, Li M, Sun X, Li J, Duan L, Hao J. Design strategies for $CeO_2$-$MoO_3$ catalysts for $DeNO_x$ and $Hg^0$ oxidation in the presence of HCl: The significance of the surface acid-base properties. Environmental Science & Technology, 2015, 49(20): 12388–12394
13. Li H, Wu S, Wu C Y, Wang J, Li L, Shih K. SCR atmosphere induced reduction of oxidized mercury over CuO-$CeO_2$/$TiO_2$ catalyst. Environmental Science & Technology, 2015, 49(12): 7373–7379
14. Wang Y, Chang H, Shi C, Duan L, Li J, Zhang G, Guo L, You Y. Novel Fe-Ce-O mixed metal oxides catalyst prepared by hydrothermal method for $Hg^0$ oxidation in the presence of $NH_3$. Catalysis Communications, 2017, 100: 210–213
15. Reddy B M, Khan A, Yamada Y, Kobayashi T, Loridant S, Volta J C. Structural characterization of $CeO_2$–$MO_2$ (M = $Si^{4+}$, $Ti^{4+}$, and $Zr^{4+}$) mixed oxides by Raman spectroscopy, X-ray photoelectron spectroscopy, and other techniques. Journal of Physical Chemistry B, 2003, 107(41): 5162–5167
16. Bera P, Patil K C, Jayaram V, Subbanna G N, Hegde M S. Ionic dispersion of Pt and Pd on $CeO_2$ by combustion method: Effect of metal–ceria interaction on catalytic activities for NO reduction and CO and hydrocarbon oxidation. Journal of Catalysis, 2000, 196(2): 293–301
17. Roy S, Marimuthu A, Hegde M S, Madras G. High rates of NO and $N_2O$ reduction by CO, CO and hydrocarbon oxidation by $O_2$ over nano crystalline $Ce_{0.98}Pd_{0.02}O_2$−δ: Catalytic and kinetic studies. Applied Catalysis B: Environmental, 2007, 71(1-2): 23–31
18. Cui L, Tang Y, Zhang H, Hector L G Jr, Ouyang C, Shi S, Li H, Chen L. First-principles investigation of transition metal atom M (M = Cu, Ag, Au) adsorption on $CeO_2(110)$. Physical Chemistry Chemical Physics, 2012, 14(6): 1923–1933
19. Lim D H, Aboud S, Wilcox J. Investigation of adsorption behavior of mercury on Au(111) from first principles. Environmental Science & Technology, 2012, 46(13): 7260–7266
20. Lim D H, Wilcox J. Heterogeneous mercury oxidation on au(111) from first principles. Environmental Science & Technology, 2013, 47(15): 8515–8522

21. Jung J E, Geatches D, Lee K, Aboud S, Brown G E Jr, Wilcox J. First-principles investigation of mercury adsorption on the α-$Fe_2O_3$ surface. Journal of Physical Chemistry C, 2015, 119(47): 26512–26518
22. Zhang B, Liu J, Zheng C, Chang M. Theoretical study of mercury species adsorption mechanism on $MnO_2$(110) surface. Chemical Engineering Journal, 2014, 256(256): 93–100
23. Zhang B, Liu J, Shen F. Heterogeneous mercury oxidation by HCl over $CeO_2$ catalyst: density functional theory study. Journal of Physical Chemistry C, 2015, 119(27): 15047–15055
24. Fabris S, Gironcol S D, Baroni S, Vicario G, Balducci G. Taming multiple valency with density functionals: A case study of defective ceria. Physical Review B: Condensed Matter and Materials Physics, 2005, 71(4): 041102
25. Da Silva J L F, Ganduglia-Pirovano M V, Sauer J, Bayer V, Kresse G. Hybrid functionals applied to rare-earth oxides: The example of ceria. Physical Review B: Condensed Matter and Materials Physics, 2007, 75(4): 045121
26. Loschen C, Carrasco J, Neyman K M, Illas F.First-principles LDA + U and GGA + U study of cerium oxides: Dependence on the effective U parameter. Physical Review B: Condensed Matter and Materials Physics, 2007, 75(3): 035115
27. Kresse G, Hafner J. Ab initio molecular dynamics for liquid metals. Physical Review B: Condensed Matter and Materials Physics, 1993, 47(1): 558–561
28. Kresse G, Furthmüller J. Efficient iterative schemes for ab initio total-energy calculations using a plane-wave basis set. Physical Review B: Condensed Matter and Materials Physics, 1996, 54(16): 11169–11186
29. Kresse G, Furthmüller J. Efficiency of ab-initio total energy calculations for metals and semiconductors using a plane-wave basis set. Computational Materials Science, 1996, 6(1): 15–50
30. Blöchl P E. Projector augmented-wave method. Physical Review B: Condensed Matter and Materials Physics, 1994, 50(24): 17953–17979
31. Perdew J P, Burke K, Ernzerhof M. Generalized gradient approximation made simple. Physical Review Letters, 1996, 77 (18): 3865–3868
32. Perdew J P, Burke K, Ernzerhof M. Generalized gradient approximation made simple. Physical Review Letters, 1997, 78 (7): 1396
33. Zhang C, Michaelides A, King D A, Jenkins S. Oxygen vacancy clusters on ceria: Decisive role of cerium f electrons. Physical Review B: Condensed Matter, 2009, 79(7): 075433
34. Fabris S, de Gironcoli S, Baroni S, Vicario G, Balducci G. Taming multiple valency with density functionals: A case study of defective ceria. Physical Review B: Condensed Matter and Materials Physics, 2005, 72(23): 237102
35. Tang W, Sanville E, Henkelman G. A grid-based Bader analysis algorithm without lattice bias. Journal of Physics Condensed Matter, 2009, 21(8): 084204
36. Sanville E, Kenny S D, Smith R, Henkelman G. Improved grid-based algorithm for Bader charge allocation. Journal of Computational Chemistry, 2007, 28(5): 899–908